Experimental and theoretical studies on the removal mechanism of formaldehyde from water by mesoporous calcium silicate

WANG ManMan, FAN BaoMin[*], WEN BianYing[*] & JIANG Chao

School of Materials Science and Mechanical Engineering, Beijing Technology and Business University, Beijing 100048, China

Most porous materials with high specific surface area and diverse internal structures possess good adsorption ability. In this work, a tremella-like mesoporous calcium silicate hydrate (CSH) with high adsorption capacity was successfully prepared via a facile hydrothermal method. The adsorption effect and adsorption mechanism of the as-prepared calcium silicate hydrate (AP-CSH) towards formaldehyde from water were investigated systematically. Results indicate that AP-CSH has high Ca/Si ratio (1.95), large specific surface area (122.83 $m^2\,g^{-1}$) and exhibits excellent adsorption capacity. The results of batch adsorption experiments show that AP-CSH can remove formaldehyde from water rapidly and effectively with the maximum removal efficiency of 98.94%. The adsorption process agrees well with the pseudo-second-order and Freundlich isotherm model. Furthermore, regeneration can be achieved by simply immersing AP-CSH in absolute ethanol and the removal efficiency can still reach about 99.50% after five cycles. The adsorption mechanism was also studied by experimental analyses and molecular dynamics simulation. Both experimental results and theoretical simulation support that formaldehyde adsorption over AP-CSH belongs to chemical adsorption.

chemical adsorption, mechanism, molecular dynamics simulation, mesoporous calcium silicate, formaldehyde

1   Introduction

Adsorption, with advantages of high efficiency and low operation cost, plays a critical role in the removal of hazards in the environment. Most porous materials with high specific surface area and diverse internal pore structures, such as activated carbon [1], diatomite [2], zeolite [3] and metal organic frameworks (MOFs) [4], have been widely used in the field of adsorption. Porous adsorbents involve both organic and inorganic specimens. Organic porous materials have excellent selective adsorption but the manufacturing process is usually complex. For instance, MOFs, as typical organic adsorbents, have excellent selective adsorption performance for some substance with the adjustable chemical composition and pore size [5]. However, the syntheses of MOFs are complicated and expensive, which limit the practical applications. Compared with most organic counterparts, inorganic adsorbents exhibit extraordinary performance in removing contaminants due to their resistance to heat- and solvent-induced swelling. Besides, with regard to cost, chemical composition and physical structure, inorganic adsorbents exhibit more commercial value for a wide range of practical applications. Nevertheless, inorganic adsorbents share the disadvantages of poor regeneration performance and insufficient adsorption efficiency. Therefore, the development of efficient inorganic adsorbents for pollutants is still challenging.

As a new inorganic adsorbent, calcium silicate with multiple structures (e.g., honeycomb, lamellar, rod-shape) has been applied in the removal of pollutants from water. Niu-

---

*Corresponding authors (email: fanbaomin@btbu.edu.cn; wenbianying@tsinghua.org.cn)

niavaite et al. [6] reported that calcium silicate with microstructure of honeycomb had been applied in the efficient removal of inorganic heavy metal ions, such as Cu^{2+}, Cr^{3+}, Co^{2+}, from wastewater. Zhou et al. [7] studied the adsorption of chloride ions using calcium silicate with different chemical compositions and found that high Ca/Si ratio could improve the adsorption capacity stemming from the intensified interaction between Ca^{2+} and Cl^-. Generally, conventional calcium silicates based on calcium carbonate and silica as raw materials, which are prepared by sintering at high temperature, could not provide satisfactory adsorption performance due to their dense structure [8]. It is noteworthy that the specimens prepared via hydrothermal method show larger specific surface area, more uniform pore size, higher adsorption ability and better regeneration performance than those of traditional calcium silicate [9]. Moreover, the application of porous calcium silicate in the removal of organic contaminants (e.g., formaldehyde) from the aqueous solution and the corresponding mechanism are not well understood.

Formaldehyde has been regarded as a highly toxic volatile organic pollutant with high chemical reactivity, and has also been classified as the human carcinogen by International Agency for Research on Cancer (IARC) [10]. In addition, as an unexpected by-product, formaldehyde can be generated from numerous industries including pharmaceutical industry [11], papermaking [12], resin preparation [13], food processing [14], and fermentation engineering [15]. Compared with its volatile gaseous state, formaldehyde in aqueous solution can be more likely to accumulate, resulting in the formation of high concentration hazards. Therefore, the removal of formaldehyde in aqueous solution should be an urgent and difficult issue in the field of environmental protection. Recently, Pásztory et al. [16] studied the formaldehyde adsorption-desorption process on poplar bark and found that the adsorption for formaldehyde was a reversible physical process, and the adsorption capacity could reach 0.9 mg g^{-1}. Zvulunov et al. [17] designed and prepared a multi-functional and self-regenerated composite material to remove formaldehyde from water; the adsorption process was in good agreement with the Langmuir model and the corresponding maximum adsorption capacity was 62 mg g^{-1}. It is expected that, most relevant adsorbents can be further improved with respect to adsorption capacity in the removal of formaldehyde from aqueous solution.

Herein, we prepared a tremella-like mesoporous calcium silicate hydrate (CSH) via a facile hydrothermal method under alkaline condition. The microstructure and the formaldehyde adsorption properties of the as-prepared calcium silicate hydrate (AP-CSH) were investigated. Combined with the physical properties analyses, molecular dynamics simulation and quantum chemical calculation were also employed to further study the adsorption mechanism for formaldehyde on AP-CSH.

2   Experimental

2.1   Materials and solutions

Powder calcium hydroxide (Ca(OH)$_2$) was obtained commercially from Fuchen Chemical Reagents Co., Ltd, Tianjin, China; soluble sodium silicate (Na$_2$SiO$_3$) was purchased from Bailingwei Technology Co., Ltd, Beijing, China. Acetamide, glacial acetic acid and acetylacetone were obtained from Komeo Chemical Reagent Co., Ltd, Tianjin, China. The formaldehyde solutions with preset concentrations were prepared by diluting concentrated solution (37 wt%, analytical reagent, Damao Chemical Reagent Works, Tianjin, China) with deionized water, and were stored in sealed bottles at 4°C. The concentrations of formaldehyde solution employed in this work were varied from 50 to 400 mg L^{-1}. Analytically pure CSH was purchased from Macklin Biochemical Technology Co., Ltd, Shanghai, China, and was characterized for comparison with AP-CSH.

2.2   Preparation of AP-CSH

AP-CSH was synthesized by the reaction between Na$_2$SiO$_3$ and Ca(OH)$_2$ via hydrothermal method in the alkaline environment, and the corresponding preparation route is presented in Figure 1. Initially, proper amount of Na$_2$SiO$_3$ was dissolved in deionized water followed by the addition of Ca(OH)$_2$ under vigorous stirring with a Ca/Si molar ratio of 1/1. Then, the obtained slurry was continuously stirred at 70°C for 4 h, in which the liquid/solid ratio (w/w) was constrained in 30/1. The slurry was transferred into a hydrothermal reactor to complete the reaction at 120°C under 1.5 MPa for 2 h at a pH of 12. After being naturally cooled to the ambient temperature (about 28°C), the resultant was vacuum dried, sieved through 900# mesh, to give product in a state of white powder.

2.3   Characterization of CSH

The morphologies of samples were captured by the scanning electron microscopy (SEM, FEG 250, Quanta FEI) operated at an accelerating voltage of 10.0 kV, and the element composition was analyzed by the attached energy-dispersive spectrometer (EDS). The X-ray diffraction (XRD) analyses were performed with PANalytical X'Pert Powder instrument using monochromatic Cu Kα radiation (λ=0.154 nm). The samples were analyzed in the 2θ angle ranging from 5° to 90° with a step size of 0.1° (2θ). Nitrogen adsorption-desorption isotherms were obtained by a SSA-6000 aperture specific surface area analyzer (Biaode Electronic Technology Co., Ltd, Beijing, China). Based on the Barrett-Joyner-Halenda (BJH) method, both the specific surface area and the pore size distribution were obtained. Fourier transform infrared reflection (FT-IR) spectra of samples were determined by a
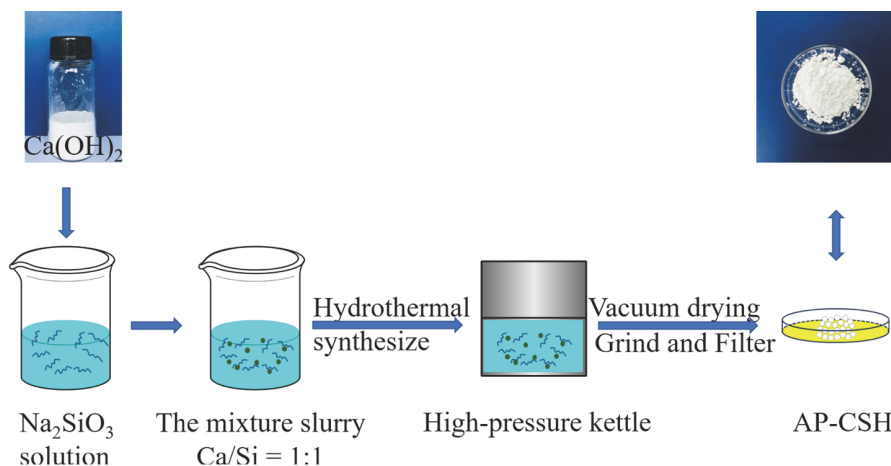
Figure 1   (Color online) Schematic illustration for the preparing route of AP-CSH.

Nicolet iN10 spectrometer (Thermo Scientific, USA) over a range of 400–4000 cm^{-1}. Thermo gravimetry (TG) analysis was performed with a Q50 thermogravimetric analyzer (TA Instruments, USA), and each specimen was heated from ambient temperature to 800°C at a heating rate of 20°C min^{-1} in a platinum crucible under nitrogen atmosphere. X-ray photoelectron spectroscopy (XPS) analysis was conducted on an ESCALAB 250 system (Thermo Fisher Scientific, USA) by employing monochromatic Mg Kα radiation (1253.6 eV) as the incident radiation source. The spectrum deconvolution was achieved using XPS Peak-Fit 4.1 software with Gaussian functions after subtraction of a Shirley background.

2.4   Adsorption studies

2.4.1   Adsorption kinetics

Adsorption kinetic studies were performed through batch adsorption experiments with different initial formaldehyde concentrations varied from 50 to 400 mg L^{-1} at 25°C by a temperature-controlled magnetic agitator. A certain amount of AP-CSH (0.4 g) was added into the conical flask, and then 50 mL formaldehyde solution with the pre-specified concentration was added under stirring. The plug of conical bottle was sealed with polyethylene film to prevent formaldehyde from volatilizing during the experiment. The mixture was stirred at 200 r/min for desired periods (15, 30, 60, 90, 120 and 180 min), and the aliquots were centrifuged, which were transferred into 25 mL test tubes with glass stoppers for concentration determination. The concentration of formaldehyde in the solution was determined by using an ultraviolet spectrophotometer (UV-2450, Shimadzu Corp., Japan) at the maximum adsorption wavelength of 271 nm based on the standard curve established in the preliminary experiment.

The equilibrium adsorption capacity (Q_e, mg g^{-1}) and removal efficiency (R, %) of formaldehyde were calculated using eqs. (1) and (2):

$$Q_e = \frac{(C_0 - C_e)v}{m}, \tag{1}$$

$$R = \frac{C_0 - C_e}{C_0} \times 100\%, \tag{2}$$

where C_0 and C_e (mg L^{-1}) represent the concentrations of formaldehyde under initial and equilibrium conditions, respectively; v (L) represents the volume of formaldehyde solution; and m (g) represents the mass of AP-CSH.

2.4.2   Adsorption thermodynamics

The effect of temperatures on the adsorption properties of AP-CSH against formaldehyde was studied by adding a certain amount of AP-CSH (0.4 g) into 50 mL formaldehyde solution (100 mg L^{-1}) at 25°C, 35°C and 45°C. After pre-specified intervals (3, 6, 9, 15, 30, 60, 90, 120 and 180 min), the adsorbent was separated from the solution by centrifugation, and the formaldehyde concentration in the residue was measured through UV spectrophotometer.

2.4.3   Adsorption isotherm

Adsorption isotherm studies were conducted by mixing 0.4 g AP-CSH with 50 mL formaldehyde solutions with different initial concentrations (50, 100, 200, 300, 400 mg L^{-1}) for 120 min at the preset temperatures (25°C, 35°C and 45°C). The formaldehyde solution was extracted from the mixture and analyzed by UV spectrophotometer at a wavelength of 271 nm. Based on the established standard curve, the formaldehyde concentration can be obtained for fitting the different isotherm models.

2.5   Computational details

2.5.1   Simulation models and molecular dynamics modeling

Molecular dynamics (MD) simulation was performed with

Forcite tool in Materials Studio 8.0 software (BIOVIA Inc., USA). According to XRD analysis, the structure of AP-CSH (wollastonite) was retrieved from American Mineralogist Crystal Structure Database [18] and cleaved parallel to (1 0 0) plane adding hydrogen atoms to the surface Si–O bonds pointing to the perpendicularly substrate. The thickness and position of the vacuum slab crystal were set as 20.00 and 1.00 Å, respectively. The dimensions of the supercell were set as a=44.00 Å, b=44.00 Å, c=22.77 Å, α=90°, β=90°, and γ=90° containing 24 crystallographic unit cells. The constructed solution layer comprised of 1000 water molecules and 10 formaldehyde molecules. Geometry optimizations were initially performed for both wollastonite structure and solution layer using the force fields of ClayFF. Afterwards, MD simulations were conducted at 298 K under Hoover Canonical ensemble NVT ensemble (constant atom number, volume and temperature kept by Nose thermostat). The simulation period lasted for 1000 ps, in which the equilibrium configurations were exported every 1 ps.

2.5.2 Quantum chemical calculation

Quantum chemical calculation was conducted in DMol3 module in terms of density function theory to reveal the charge distribution of formaldehyde and point out the potential interactive sites for formaldehyde on AP-CSH. The optimized structure of formaldehyde was obtained with the help of generalized gradient approximation (GGA) and Becke-Lee-Yang-Parr (BLYP). Then, the charge distribution and molecular electrostatic potential (MEP) of formaldehyde were calculated.

2.6 Desorption and regeneration

Desorption study was carried out in a similar way and was followed by adsorption experiments. After the adsorption of formaldehyde (the initial formaldehyde concentration 100 mg L^{-1}, stirring speed 200 r/min, temperature 25°C), AP-CSH was regenerated by immersing in absolute ethanol for 10 min and recovered by simple filtration at ambient temperature (25°C). This procedure was repeated five times, generating five desorption steps. The concentration of residual formaldehyde solution was determined through UV spectrophotometer.

3 Results and discussion

3.1 Characterization of calcium silicate

The AP-CSH obtained through hydrothermal synthesis under alkaline conditions was characterized by XRD, FT-IR, SEM/EDS. The analytical grade CSH (AR-CSH) was also characterized for contrast.

It is clear in Figure 2(a) that the XRD pattern of AR-CSH

exhibits a series of sharp peaks, which corresponds to wollastonite ($Ca_2SiO_4 \cdot H_2O$, PDF 29-0373). In contrast, AP-CSH shows few peaks in the pattern, in which the peaks located at 29.95° and 49.90° also correspond to wollastonite ($CaSi_2O_5$, PDF 29-0156). In light of the fitting process, the crystallinity of AR-CSH and AP-CSH was calculated as 69.80% and 31.22%, respectively. Hence, AP-CSH possesses a property of low-crystallinity compared with AR-CSH. This also explains the reason for less peaks emerged in the XRD pattern of AP-CSH than that of AR-CSH. Similar observation was obtained by Guan and Zhao [19]. Figure 2(b) presents FT-IR spectra of AR-CSH and AP-CSH. The characteristic adsorption bands near 3430, 1630, 970, 450 cm^{-1} exist in both spectra for AR-CSH and AP-CSH. The band near 3426 cm^{-1} (AP-CSH) and 3431 cm^{-1} (AR-CSH) can be attributed to the stretching vibration of O–H bond. A broader peak in the spectrum is observed for AP-CSH than for corresponding AR-CSH, which indicates the higher number of hydroxyls in AP-CSH [20]. The abundant hydroxyls contained in the adsorbent are prone to chelate pollutants with high intensity of hydrogen bond [21]. In addition, the band at 1645 cm^{-1} is due to H–O–H bending vibration of H_2O [22]. The bands in the range of 1400–1500 cm^{-1} correspond to the asymmetric stretching of CO_3^{2-} [22,23]. The adsorption band at 967 cm^{-1} points out that a single silicate atom and two oxygen atoms are bridging in the structure, while the band at 817 cm^{-1} stems from silicate with one bridging oxygen atom [24]. The adsorption bands at 457 and 667 cm^{-1} can be assigned to the bending vibration of Si–O–Si [25]. Based on the results of XRD and FT-IR, it is reasonable to assume that CSH has been successfully prepared via our designed route.

Displayed in Figure 2(c) and (e) are morphologies of AR-CSH and AP-CSH, and the corresponding EDS spectra are shown in Figure 2(d) and (f), respectively. As can be observed in Figure 2(c), AR-CSH presents a shape of irregularly aggregated rod-like particles; while AP-CSH exhibits tremella-like shape with a robust porous structure, which favors the adsorption of pollutants in the aqueous solution. According to EDS spectra, Ca/Si mass ratio of AP-CSH (1.95) is higher than that of AR-CSH (1.56). In general, the hydroxyl group linkage in CSH is in the form of Ca–OH or Si–OH, and higher Ca/Si mass ratio and lower crystallinity are related to more Ca–OH linkages, which might bond the adsorbate molecules with high strength [19].

The pore size distribution and specific surface area of samples were further clarified through nitrogen adsorption-desorption isotherms and the results are given in Figure 2(g) and (h). In Figure 2(g), isotherms of both AR-CSH and AP-CSH can be categorized as typical type of IV according to IUPAC classification, in which adsorption curve is not consistent with the desorption curve and thus the hysteresis loop appears [23]. The hysteresis loop of AP-CSH is larger than that of AR-CSH indicating more robust porous struc-
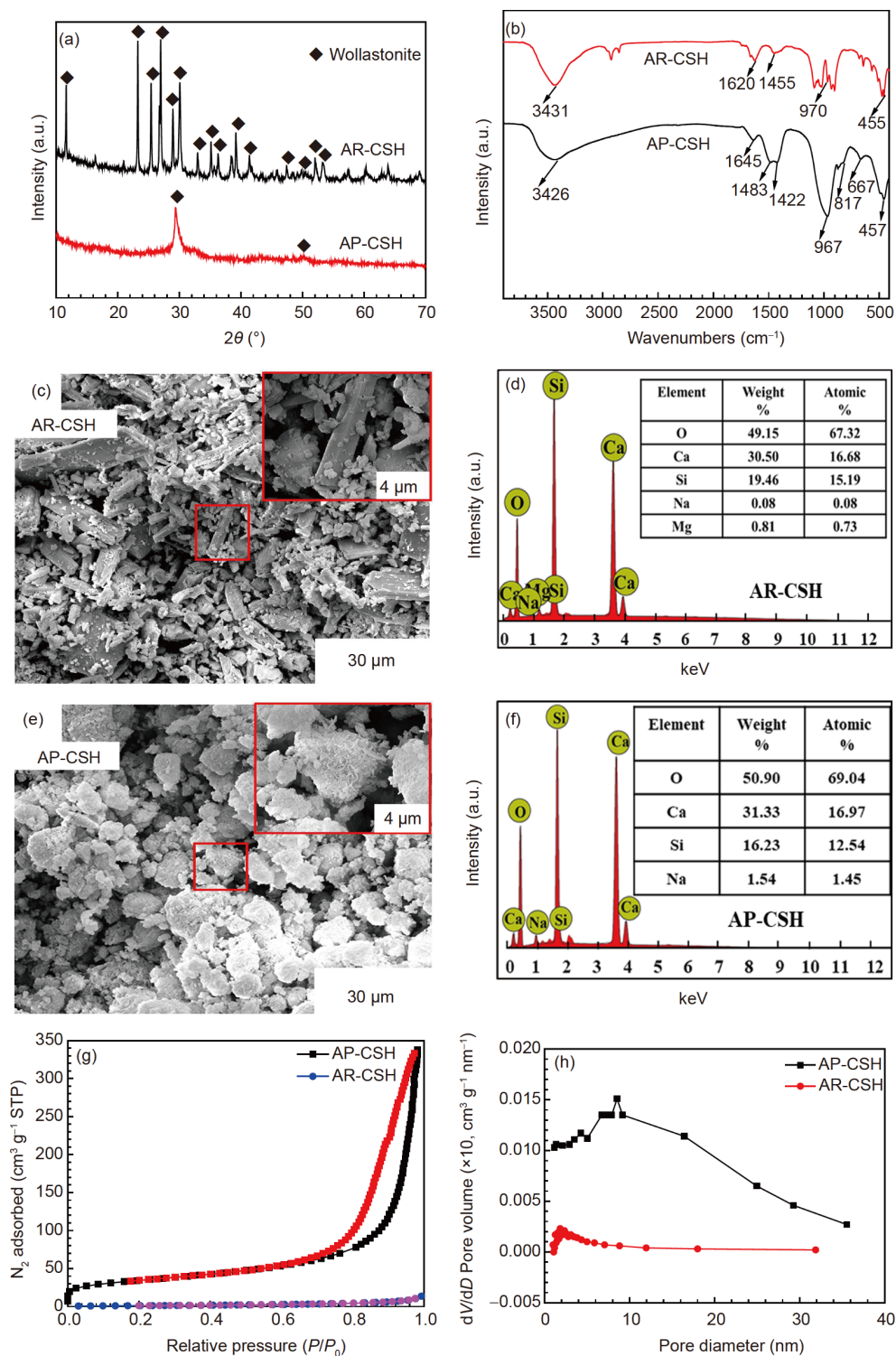
Figure 2 (Color online) Comparison of as-prepared calcium silicate and analytically pure counterpart. (a) X-ray diffraction patterns; (b) FT-IR spectra; (c) and (e) morphologies; (d) and (f) elemental composition; (g) nitrogen adsorption-desorption isotherms; (h) pore size distributions.

ture. This observation may be credited to the more irregular particle stacking of AP-CSH than that of AR-CSH verified by Figure 2(c) and (e) as well. In Figure 2(h), the pore size distribution of AP-CSH is broader than that of AR-CSH along with the larger pore volume. The pore diameter, spe-

cific surface area, and pore volume of both samples are tabulated in Table 1. AP-CSH owns an average pore diameter of 8.56 nm validating the mesoporous property. In addition, large pore volume of AP-CSH could ensure the excellent adsorption capacity towards pollutants in aqueous solution.

Table 1 Structural properties of AR-CSH and AP-CSH

Sample	Specific surface area ($m^2\,g^{-1}$)	Average pore diameter (nm)	Pore volume ($cm^3\,g^{-1}$)
AR-CSH	3.82	11.01	0.02
AP-CSH	122.83	8.56	0.53

3.2 Adsorption kinetics

The kinetic studies were conducted to gain insights into the adsorption ability of AP-CSH towards formaldehyde. The time-dependent adsorption curves of AP-CSH against formaldehyde with different initial concentrations are shown in Figure 3. It can be observed in Figure 3(a) that the adsorption of formaldehyde is rapid in the initial 5 min, and then the adsorption rate levels off thereafter and reaches equilibrium after 60 min. The fast adsorption rate may be credited to the inherent mesoporous structure of AP-CSH, in which the active adsorption sites are mainly spread over the outer surface and as a result the diffusion resistance of mass transfer during adsorption might be negligible [26]. Besides, high formaldehyde concentration also facilitates its tight binding with AP-CSH owing to the intense concentration gradient. In addition, with the adsorption proceeding, both the pollutant concentration and the active adsorption sites were reduced. The reduced concentration gradient might be unfavorable for formaldehyde diffusing towards the surface of AP-CSH, which is responsible for the adsorption equili-

brium in the remaining period.

Three adsorption kinetic models including pseudo-first-order, pseudo-second-order and intraparticle diffusion models were employed to predict the kinetics of formaldehyde adsorption process by AP-CSH. These models are given as follows:

$$\ln(Q_e - Q_t) = \ln Q_e - k_1 t, \tag{3}$$

$$\frac{t}{Q_t} = \frac{1}{k_2 Q_e^2} + \frac{1}{Q_e} t, \tag{4}$$

$$Q_t = k_{int} t^{1/2} + \theta, \tag{5}$$

where Q_e and Q_t are the equilibrium and instant adsorption amount (mg g^{-1}), respectively; k_1 (min^{-1}) and k_2 (g mg^{-1} min^{-1}) are the rate constants of pseudo-first-order and pseudo-second-order model, respectively; k_{int} (mg g^{-1} min^{-1}) is a constant related to the diffusion coefficient in intraparticle diffusion model; θ (mg g^{-1}) is the intercept for the intraparticle diffusion model.

Based on eqs. (3)–(5), the calculated results are presented in Figure 3(b)–(d), respectively. The relevant kinetic parameters were calculated from the fitted results and tabulated in Table 2. Compared with pseudo-first-order and intraparticle diffusion models, the pseudo-second-order kinetic model exhibits the best fitting level with the correlation coefficients quite close to unity. Hence, it is accepted that both the binding sites spread over the outer surface and within the interior of AP-CSH are readily available for for-
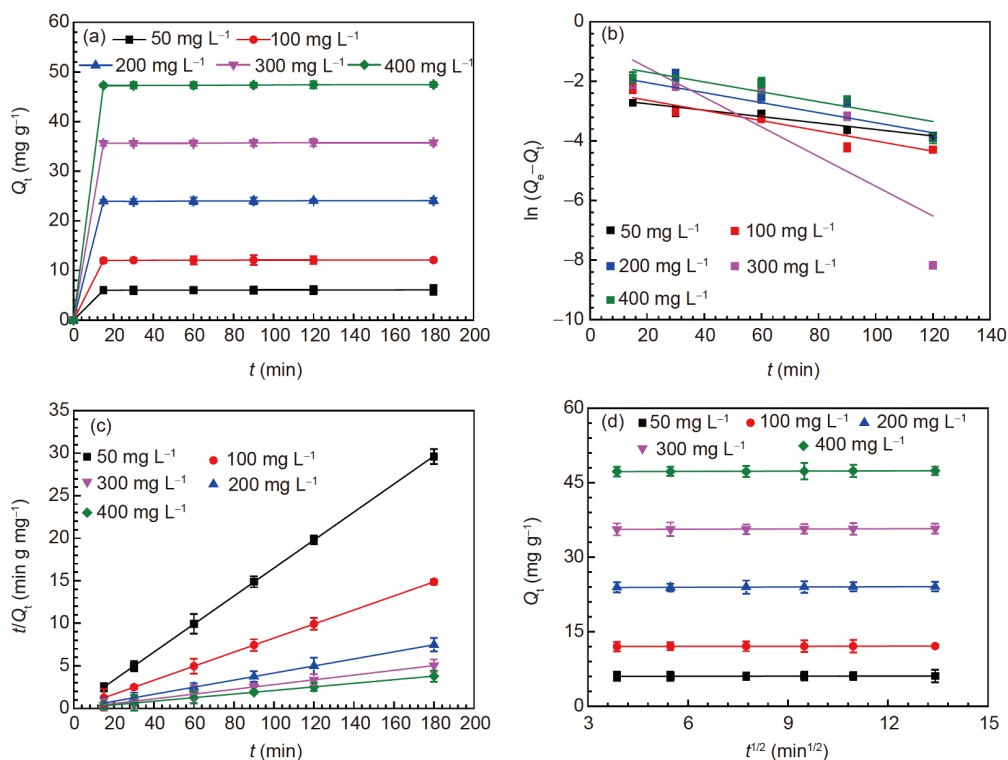

Figure 3 (Color online) (a) Effect of contact time on formaldehyde adsorption by AP-CSH; (b) the linear fit with pseudo-first-order model; (c) the linear fit with pseudo-second-order model; (d) intraparticle diffusion model.

Table 2　Parameters of adsorption kinetic fitting results on formaldehyde by AP-CSH at gradient concentration

Parameter	Initial concentration of formaldehyde (mg L^{-1})				
	50	100	200	300	400
Pseudo-first-order model					
Q_e (mg g^{-1})	0.08	0.11	0.22	0.65	0.27
k_1 (min^{-1})	0.0105	0.0192	0.0175	0.0502	0.0183
R^2	0.9351	0.8897	0.7994	0.5845	0.7730
Pseudo-second-order model					
Q_e (mg g^{-1})	6.08	12.11	24.09	35.76	47.43
k_2 (g mg^{-1} min^{-1})	0.47	0.47	0.20	0.23	0.17
R^2	0.9999	1	1	1	1
Intraparticle diffusion model					
θ (mg g^{-1})	5.98	11.98	23.86	35.55	47.18
k_{int} (mg g^{-1} min^{-1})	0.01	0.01	0.02	0.01	0.02
R^2	0.9628	0.7970	0.7905	0.8580	0.9080
Experimental value Q_e (mg g^{-1})	6.08	12.11	24.07	35.74	47.42

maldehyde adsorption. Moreover, the theoretical values of Q_e (6.08, 12.11, 24.09, 35.76, 47.43 mg g^{-1}) gained from pseudo-second-order model are almost the same as those obtained from experiments, which also demonstrates that the pseudo-second-order model is suitable for the formaldehyde adsorption by AP-CSH.

3.3　Adsorption thermodynamics

The effect of temperature on the adsorption capacity of formaldehyde by AP-CSH was studied at 298, 308, and 318 K (Figure 4). As can be seen in Figure 4(a), the adsorption capacity of formaldehyde progressively increases with the elevated temperature implying an endothermic adsorption process [27]. The temperature-related thermodynamics parameters, i.e. standard Gibbs free energy change (ΔG^0), standard enthalpy change (ΔH^0) and standard entropy change (ΔS^0), were calculated through eqs. (6) and (7), which are summarized in Table 3.

$$\Delta G^0 = -RT\ln K_c, \tag{6}$$

$$\ln K_c = \frac{\Delta S^0}{R} - \frac{\Delta H^0}{RT}, \tag{7}$$

where K_c is the adsorption equilibrium distribution constant and it is calculated by $K_c = C_{ae}/C_e$, where C_{ae} is the amount of adsorbed formaldehyde (mg L^{-1}) and C_e is the equilibrium concentration (mg L^{-1}); T is the temperature in Kelvin. The ΔG^0 is calculated by eq. (6) at different temperatures; ΔH^0 and ΔS^0 can be calculated via van't Hoff equation from the intercept and slope by plotting $\ln K_c$ versus $1/T$.

All the values of ΔG^0 in Table 3 are negative indicating a spontaneous adsorption of formaldehyde by AP-CSH [28]. Moreover, the value of ΔG^0 becomes more negative with the increase of temperature, which reveals that high temperature is favorable to the adsorption process [29]. The positive sign of ΔH^0 reveals the endothermic nature of adsorption process again. Meanwhile, a rate controlling step of chemisorption can be also featured by the positive value of ΔH^0 [30,31]. The magnitude of ΔH^0 is the criteria for identifying the type
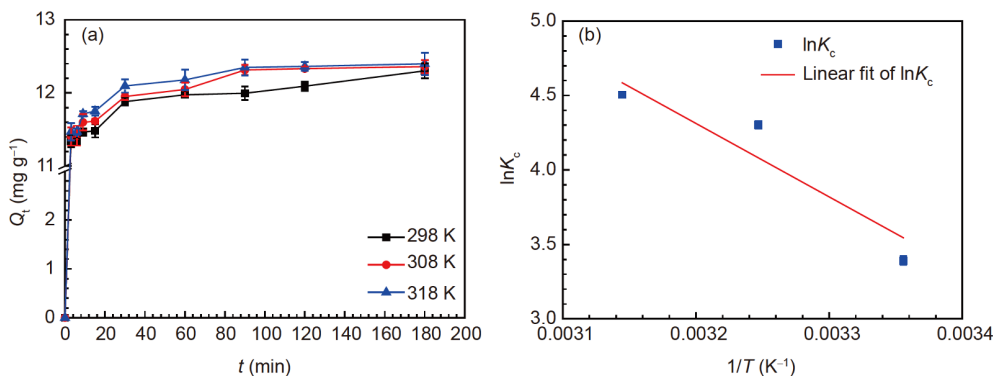

Figure 4　(Color online) Adsorption thermodynamics for formaldehyde on AP-CSH. (a) Effect of temperature; (b) plot of $\ln K_c$ versus $1/T$ (Sample dosage = 0.4 g/50 mL, C_0=100 mg L^{-1}, adsorption time = 120 min).

Table 3 Thermodynamics parameters for the adsorption of formaldehyde on AP-CSH

T (K)	ΔG^0 (kJ mol^{-1})	ΔH^0 (kJ mol^{-1})	ΔS^0 (J mol^{-1} K^{-1})
298	−8.40		
308	−11.02	41	167.04
318	−11.91		

of adsorption (i.e., chemisorption or physisorption). The value of ΔH^0 of physisorption is usually less than 4.2 kJ mol^{-1}, whilst ΔH^0 value for chemisorption is usually over 21 kJ mol^{-1} [32]. Therefore, the adsorption of formaldehyde by AP-CSH in this work can be categorized as a chemical process, in which strong interactions exist between adsorbate and adsorbent. The positive value of ΔS^0 discloses the increased randomness at solid/solution interface, which can be explained by the release of hydration H_2O during adsorption [33]. Owing to the solvation effect [34], formaldehyde molecules are in the solvation form with surrounding water molecules. As the adsorption proceeds, formaldehyde molecules are chelated by functional groups of AP-CSH, and as a result, water molecules are released and diffused in the bulk solution leading to the increase of ΔS^0 [35].

3.4 Adsorption isotherms

The adsorption isotherm is crucial for describing the ad-

sorption equilibrium state, which provides the basic information about thermodynamic properties [28,36]. The experimental data were fitted to the typical adsorption isotherms including Langmuir, Freundlich and Temkin models, and the linear forms of three adsorption isotherms can be expressed by the following equations:

$$\frac{C_e}{Q_e} = \frac{1}{Q_{max}K_L} + \frac{C_e}{Q_{max}}, \tag{8}$$

$$\ln Q_e = \ln K_F + \frac{1}{n}\ln C_e, \tag{9}$$

$$Q_e = B\ln K_T + B\ln C_e, \tag{10}$$

where C_e (mg L^{-1}) is the equilibrium concentration of formaldehyde; Q_e (mg g^{-1}) is the equilibrium adsorption capacity; Q_{max} (mg g^{-1}) is the maximum adsorption capacity; K_L (L mg^{-1}) is the Langmuir constant relevant to the affinity of binding site; K_F ((mg g^{-1}) (mg L^{-1})$^{1/n}$) and $1/n$ are the Freundlich constants that are associated with the adsorption capacity and the adsorption intensity; K_T (mg g^{-1}) is the Temkin isotherm coefficient; B (J mol^{-1}) is the Temkin coefficient related to the adsorption heat.

The linear Langmuir, Freundlich and Temkin isotherms are shown in Figure 5 and the corresponding parameters are displayed in Table 4. It is clear from the figure that the adsorption capacity increases as the initial formaldehyde concentration increases at each temperature level. In addition, adsorption capacity increases with the temperature,
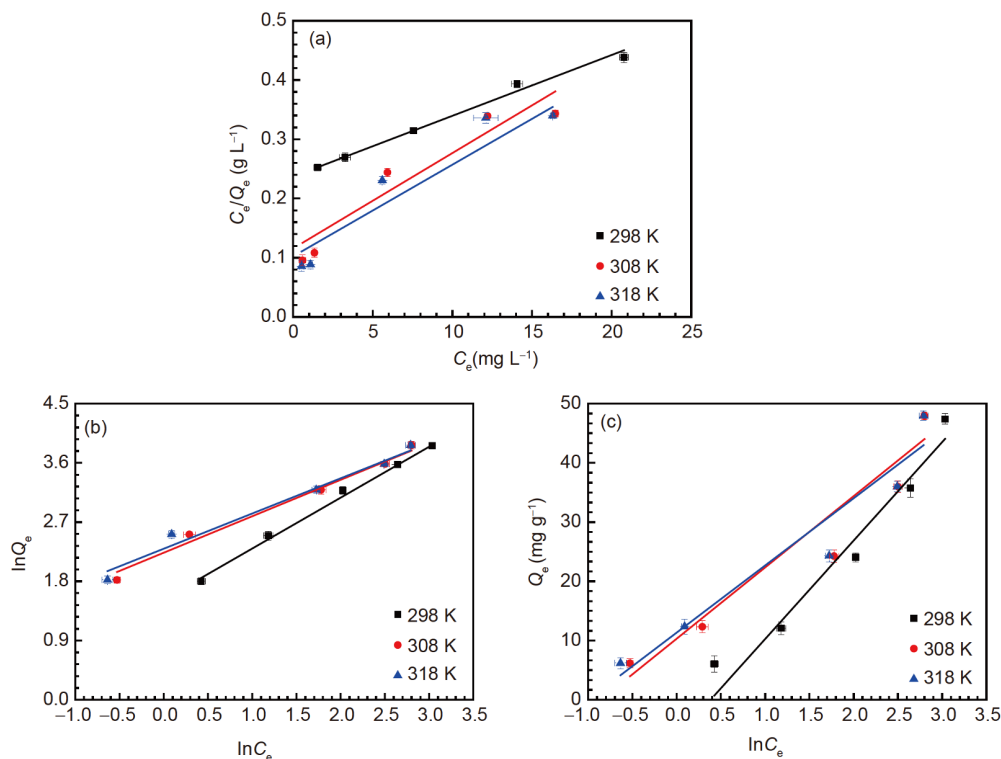

Figure 5 (Color online) Adsorption isotherms for formaldehyde on AP-CSH. (a) Langmuir isotherm; (b) Freundlich isotherm; (c) Temkin isotherm (initial concentration = 100 mg L^{-1}, adsorbents dosage = 0.4 g/50 mL).

Table 4 Isotherm parameters for the adsorption of formaldehyde on AP-CSH

Adsorption isotherm	Parameters	Temperature (K)		
		298	308	318
Langmuir	Q_{max} (mg g^{-1})	100.2	59.84	57.21
	K_L (L mg^{-1})	0.0417	0.1605	0.1908
	R_L^2	0.9860	0.8937	0.8976
Freundlich	n	1.28	1.74	1.83
	K_F ((mg g^{-1}) (mg L^{-1})$^{1/n}$)	4.5922	9.1037	9.8686
	R_F^2	0.9942	0.9834	0.9733
Temkin	B (J mol^{-1})	15.54	11.42	10.93
	K_T (mg g^{-1})	0.7806	2.3402	2.7936
	R_T^2	0.9437	0.9033	0.9060
Experimental value	Q (mg g^{-1})	47.40	47.94	47.96

which reveals the endothermic nature of adsorption process [37]. The enhanced adsorption capacity associated with the initial formaldehyde concentration indicates that the adsorption is favorable at high concentration. These results are in accordance with the kinetic analysis. Among all the models, Freundlich isotherm shown in Figure 5(b) owns the best fitting level owing to the highest correlation coefficients (0.9942, 0.9834, and 0.9733). This model is frequently used to describe the multilayer adsorption on the non-uniform surfaces such as AP-CSH.

3.5 Adsorption mechanism

3.5.1 Physical properties analysis

In order to identify the possible adsorption mechanism, the physical properties of AP-CSH before and after adsorption are summarized in Figure 6. As shown in Figure 6(a), compared with AP-CSH before adsorption, AP-CSH after formaldehyde adsorption exhibits more peaks in its diffraction pattern: the new calcite phase (PDF 17-0763) is shown apart from the original wollastonite phase. Furthermore, for AP-CSH after formaldehyde adsorption, the intensity of the peak at 2θ=29.48º and the crystallinity (47.03%) are extremely higher than that of original AP-CSH. This finding confirms that strong chemical adsorption other than physical interactions occurs during the formaldehyde adsorption by AP-CSH [38].

The FT-IR spectra of AP-CSH before and after formaldehyde adsorption are shown in Figure 6(b). The typical bands of FT-IR spectra at 2920 and 2847 cm^{-1} correspond to the C–H stretching vibration of formaldehyde [30]. The appearance of C–H stretching vibration confirms the adsorption of formaldehyde on AP-CSH.

Thermal properties for AP-CSH before and after formaldehyde adsorption were investigated by TG, and the corresponding curves are shown in Figure 6(c) and (d). It can be seen in Figure 6(c) and (d) that the total weight loss rate of

AP-CSH after adsorption (19.65%) is higher than that of the sample before adsorption (15.68%). The increase of weight loss rate further proves the adsorption of formaldehyde on AP-CSH. For the differential thermal analysis (DTA) curves of AP-CSH before adsorption shown in Figure 6(c), the initial endothermic peak at around 117°C corresponds to the loss of physical adsorption water; while the crystal water is removed at about 400°C. The successive endothermic peaks at 638°C and 719°C are responsible for the staged decomposition of Ca(OH)$_2$ impurity contained in AP-CSH [39]. For DTA curves of AP-CSH after formaldehyde adsorption, the loss of adsorbed and crystal water occurs at 116°C and 397°C, respectively. It is noteworthy that the endothermic peak centered at 664 °C related to the decomposition of Ca(OH)$_2$ is more intensive than that for the sample before adsorption, which may be caused by the loss of formaldehyde adsorbed throughout the pores on the surface and inside AP-CSH. The removal of formaldehyde at a relative high temperature further supports chemisorption of formaldehyde on AP-CSH.

SEM and EDS determinations were carried out to examine the variation in morphology and element contents of AP-CSH before and after formaldehyde adsorption, and the results are shown in Figure 7. It is clear that the dimension of AP-CSH before adsorption shown in Figure 7(a) is much smaller than that of the sample after adsorption given in Figure 7(c). This might be ascribed to the chemical interaction between formaldehyde and AP-CSH, which would lead to the agglomeration of fine particles and yield the crimp lamellar structure [40,41]. Furthermore, compared with the EDS spectrum before adsorption, the significant increase of carbon content is a direct evidence for the adsorption of formaldehyde on AP-CSH.

3.5.2 XPS analysis

In order to gain further insight into the formaldehyde adsorption mechanism by AP-CSH, the adsorbents before and
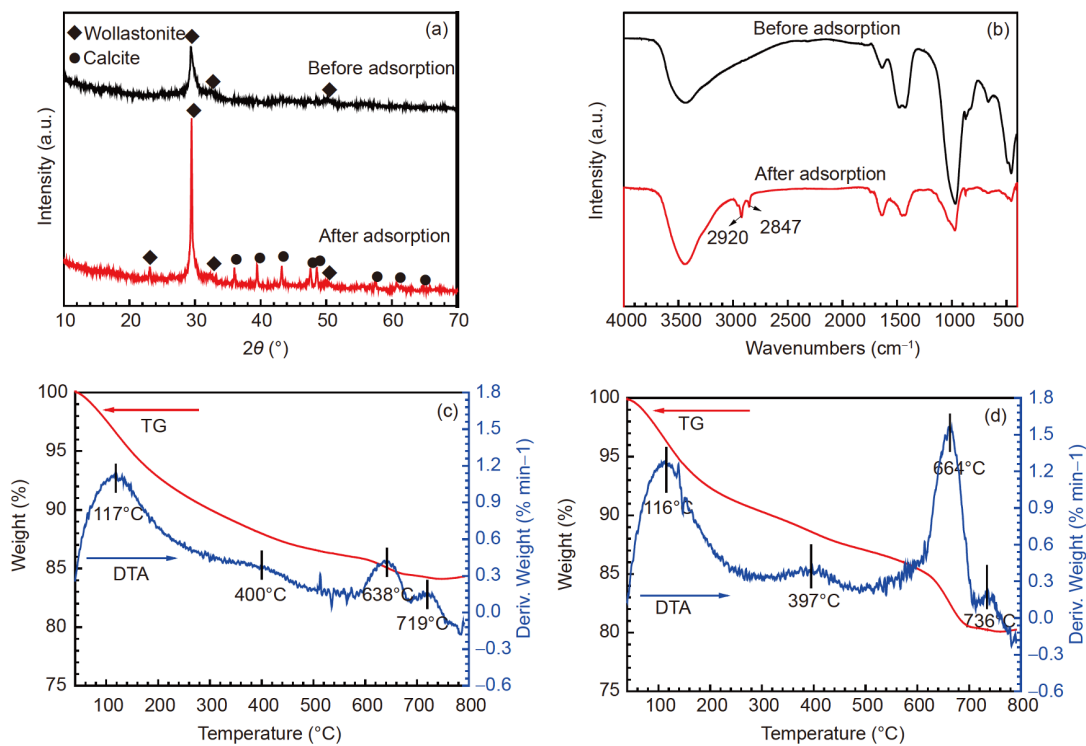
Figure 6   (Color online) Physical properties of the AP-CSH before and after formaldehyde adsorption. (a) XRD diffraction patterns; (b) FT-IR spectra; (c) TG and DTA curves of AP-CSH before formaldehyde adsorption; (d) TG and DTA curves of AP-CSH after formaldehyde adsorption.
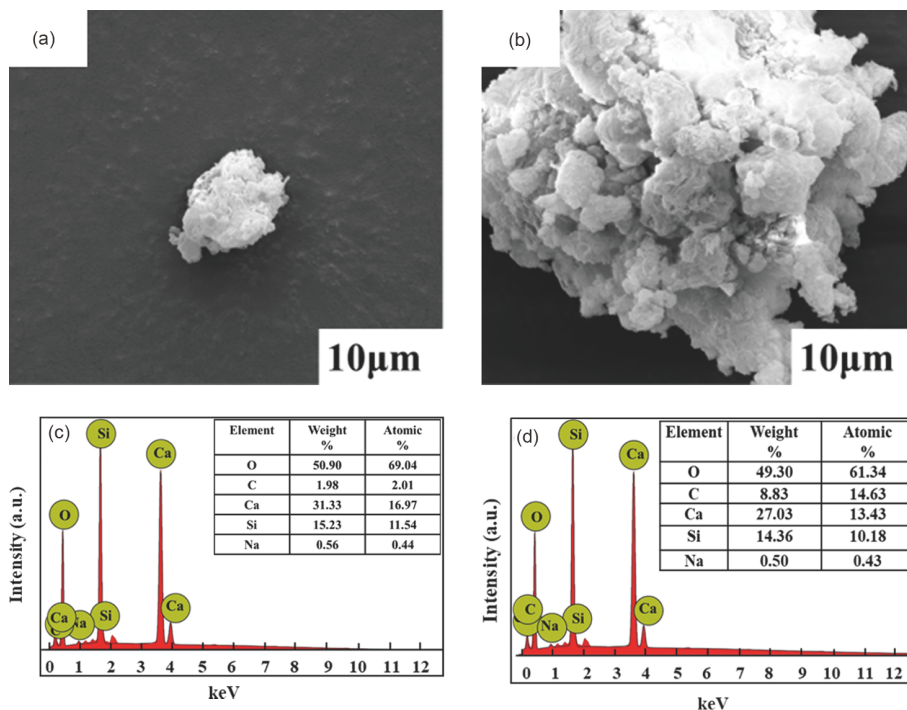

Figure 7   (Color online) SEM images and EDS spectra of AP-CSH before ((a), (c)) and after ((b), (d)) formaldehyde adsorption.

after formaldehyde adsorption were analyzed by XPS technique. Figure 8 shows the typical XPS survey spectra of AP-CSH before and after the formaldehyde adsorption. The signals of Na 1s, O 1s, C 1s, Si 2p and Ca 2p are detected in both of the spectra for AP-CSH before and after adsorption.

The high-resolution deconvolution spectra for O 1s, C 1s, Si 2p and Ca 2p of AP-CSH before adsorption are summarized in Figure 9. The spectrum of O 1s in Figure 9(a)
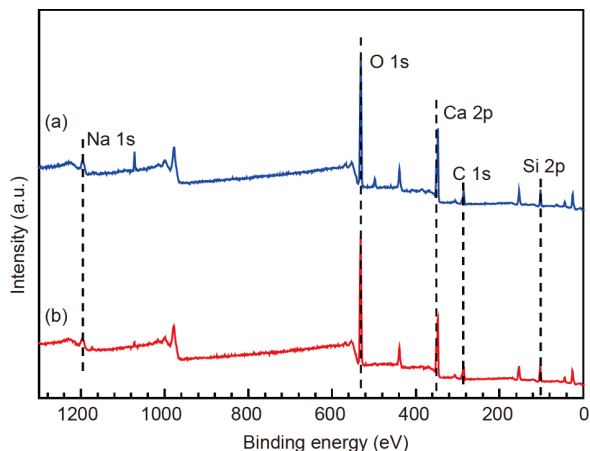
Figure 8 (Color online) XPS wide survey spectra of AP-CSH before (a) and after (b) formaldehyde adsorption.

shows four peaks at 530.20, 531.53, 532.15 and 532.61 eV and these peaks can be assigned to Ca–O, Ca–OH, O–C and O–Si bonds, respectively [42]. In the spectrum of C 1s in Figure 9(b), the peaks located at 284.78 and 286.59 eV can be ascribed to C–H and C–O, respectively; besides, the peak located at 289.52 eV represents CO_3^{2-} of Na_2CO_3 [43]. In Figure 9(c), the spectrum of Si 2p exhibits three peaks at 101.08, 101.75 and 102.47 eV corresponding to Si–H, Si–C and Si–O, respectively [42]. With respect to the Ca 2p spectrum shown in Figure 9(d), the peak centered at

346.43 eV is attributed to calcium hydroxide; the peak at 347.13 eV can be assigned to the Ca–O bond of $CaSiO_3$; and the peak at 350.34 eV is in agreement with the reports of CaO [44].

Figure 10 shows the high-resolution spectra for O 1s, C 1s, Si 2p and Ca 2p of AP-CSH after formaldehyde adsorption. Compared with the deconvolution spectra shown in Figure 9, the spectra in Figure 10 for AP-CSH after formaldehyde adsorption exhibit obvious differences embodied in O 1s and C 1s shown in Figure 10(a) and (b), respectively. Remarkably, the additional peaks at 532.80 eV in Figure 10(a) and 285.47 eV in Figure 10(b) denote the adsorption of formaldehyde on AP-CSH due to the emergence of carbonyl group (–C=O) [42]. In addition, a 0.5 eV binding energy difference is observed since the peak of Si 2p shifted from 102.47 to 102.99 eV as shown in Figure 10(c). According to the conclusion of Hu and co-workers [45], the binding energy of different atoms before and after chemical adsorption could result in a 0.5 eV or higher shift. Therefore, formaldehyde should be chemically attached on silicon-based groups, which agrees well with the adsorption thermodynamics analyses.

3.6   Theoretical calculations

MD simulation was applied to supporting the adsorption mechanism of AP-CSH towards formaldehyde in the aqu-
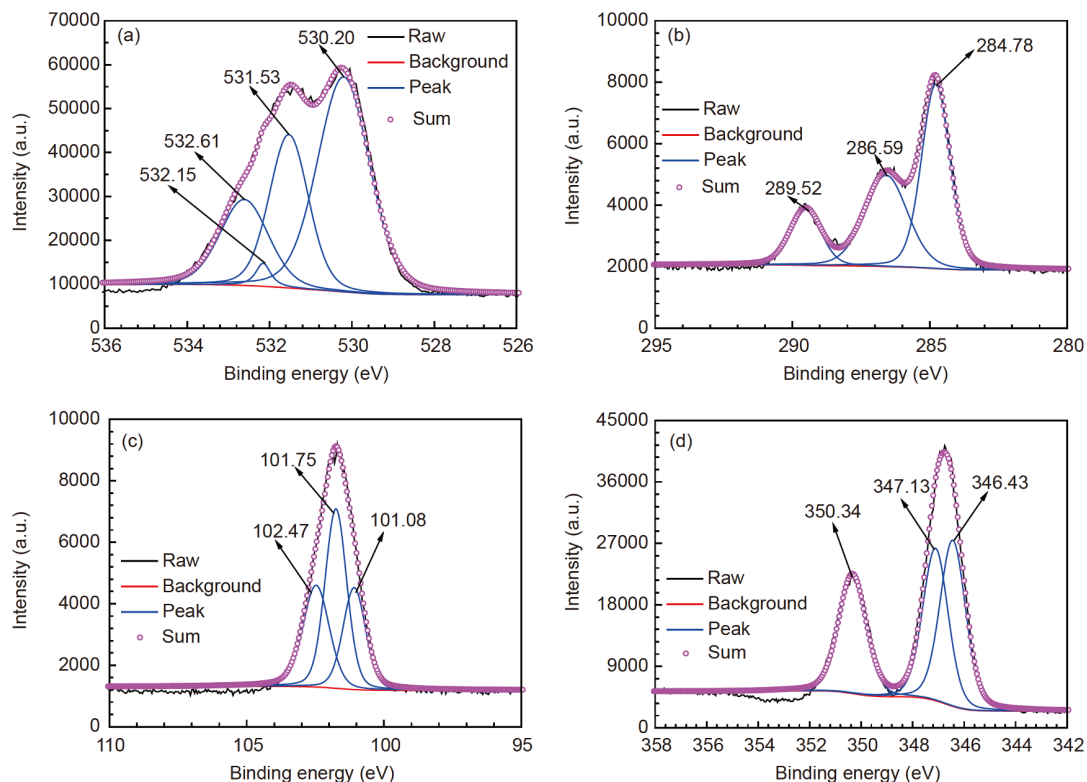

Figure 9 (Color online) High-resolution spectra of AP-CSH. (a) O 1s; (b) C 1s; (c) Si 2p; (d) Ca 2p.
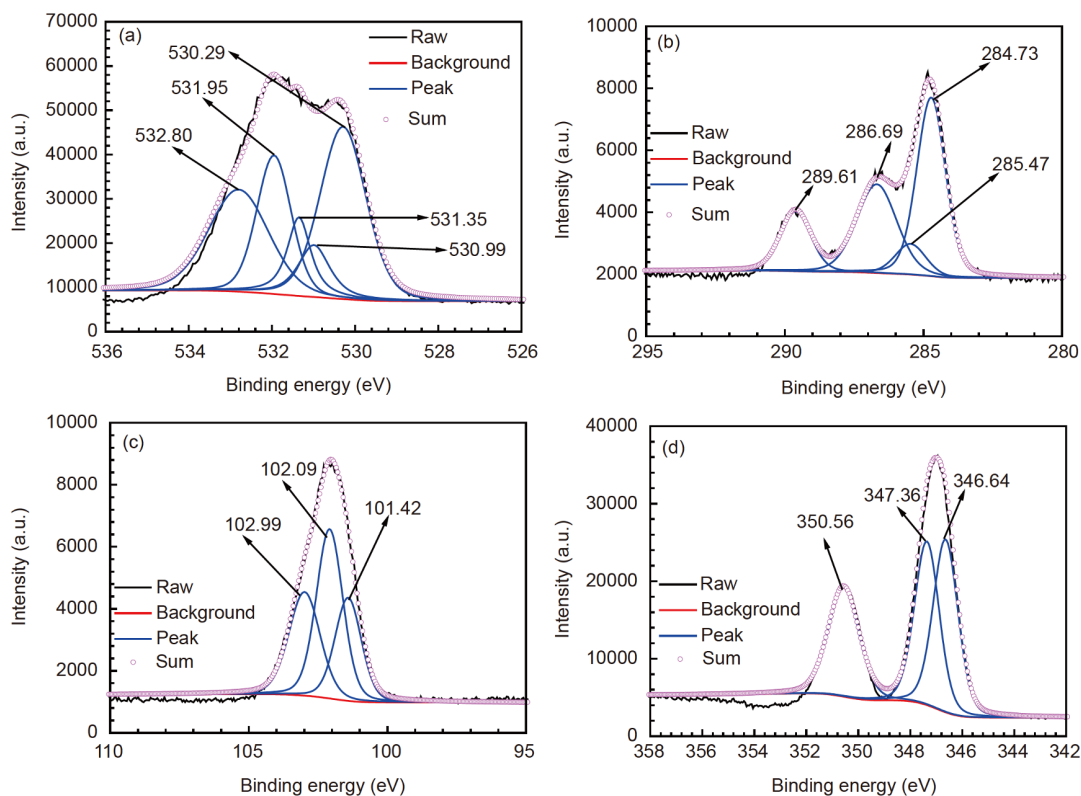
Figure 10   (Color online) High-resolution spectra of AP-CSH after formaldehyde adsorption. (a) O 1s; (b) C 1s; (c) Si 2p; (d) Ca 2p.

eous solution. The simulated results for the adsorption process are shown in Figure 11(a) and (b). As depicted in Figure 11(a), the location of formaldehyde molecules in the simulation layer box shows closer distance to the wollastonite layer than that of the initial state. Moreover, all formaldehyde molecules exhibit perpendicular adsorption orientation with high electronegativity oxygen connecting to the groups on AP-CSH. Therefore, the electronegative oxygen of formaldehyde molecule can be the active site for the interaction with AP-CSH. It can be seen in Figure 11(c) and (d) that the equilibrium configuration can be reached at the end of simulation process for the steady temperature and energy fluctuations after 1000 ps simulation. Radial density function (RDF) could be used to clarify the comprehensive property of covalent bond in the simulation box, and the position of the first maximum indicates the nearest distance between atoms [46]. In Figure 11(e) and (f), the interaction between AP-CSH and formaldehyde was analyzed in different systems. It can be noted that the first interaction shell peaks are found at 2.83 and 3.23 Å, respectively, which are both less than 3.5 Å; it proves the forming of new bonding state by coupling, and thus chemisorption exists in formaldehyde and AP-CSH [47]. Furthermore, compared with the RDF of Ca–O, the RDF of Si–O shows closer distance (2.83 Å) indicating the stronger interaction between silicon and oxygen atoms than that between calcium and oxygen atoms.

The adsorption ($E_{adsorption}$, kJ mol^{-1}) and binding energies ($E_{binding}$, kJ mol^{-1}) of the adsorption process of formaldehyde by AP-CSH were calculated by using the following equations:

$$E_{adsorption} = E_{total} - (E_{adsorbate+solution} + E_{AP\text{-}CSH}), \tag{11}$$

$$E_{binding} = -E_{adsorption}, \tag{12}$$

where E_{total} (kJ mol^{-1}) is the total energy of the system; $E_{adsorbate+solution}$ (kJ mol^{-1}) is the systematic energies for formaldehyde and solution; $E_{AP\text{-}CSH}$ (kJ mol^{-1}) is the energy of AP-CSH. The notably negative value of $E_{adsorption}$ (-98.24 kJ mol^{-1}) indicates the favorable interaction and chemisorption nature [48]; meanwhile, the positive value of $E_{binding}$ proves the tight binding force between AP-CSH and formaldehyde.

Based on the density function theory, quantum chemical calculation was performed to further clarify the interaction mechanism between AP-CSH and formaldehyde. The optimal structure, Mulliken charge and map of molecular electrostatic potential of formaldehyde are shown in Figure 12. In Figure 12(a), all the negative charges are concentrated on the oxygen atom, which could be deemed as the active center during adsorption. The result is in accord with the outcome of MD simulation: chelating interaction occurs between electronegative oxygen and silicon groups of AP-CSH.
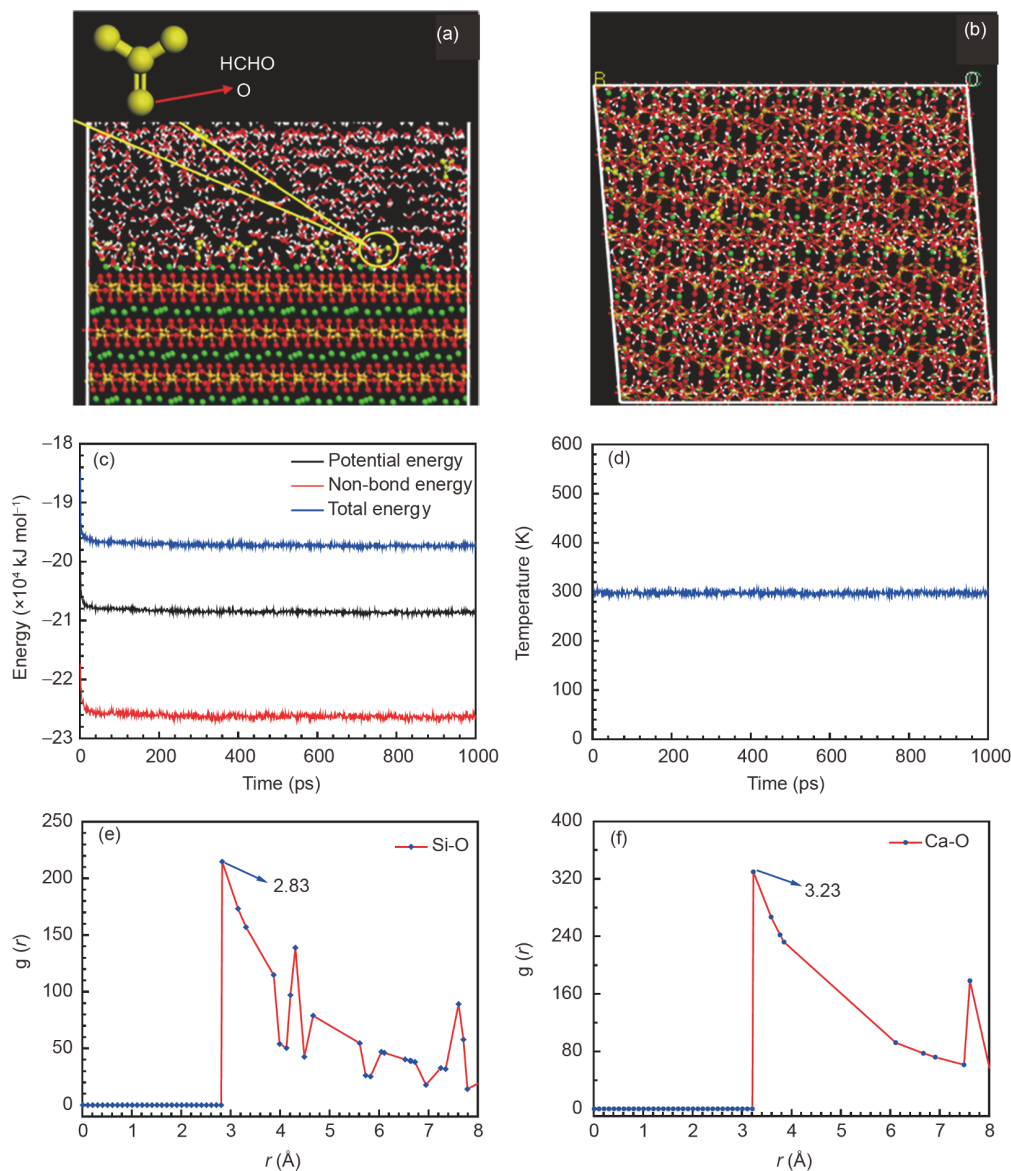
Figure 11   (Color online) Adsorption process of formaldehyde on AP-CSH (a) side view and (b) top view; energy (c) and temperature (d) fluctuation curves obtained from molecular dynamics simulation; RDF curves between AP-CSH and formaldehyde: (e) Si–O and (f) Ca–O.

Esrafili and Dinparast [49] obtained a similar conclusion, when reporting the formation of Si–O bond between Si-decorated graphene oxide and formaldehyde molecule.

3.7 Desorption and regeneration

Desorption is essential to the evaluation of the recoverability of adsorbents. Through desorption test, the nature of adsorption can be further elucidated [30]. In this study, AP-CSH after the formaldehyde adsorption was regenerated by a convenient method of immersion in absolute ethanol at ambient temperature (25°C). The regeneration results are shown in Figure 13. According to this figure, the removal efficiency for formaldehyde can still reach about 99.50% after five adsorption-desorption cycles. In contrast to the energy intensive and degradative regeneration for the regeneration process reported elsewhere [50], AP-CSH possesses excellent regeneration performance, which might result from the fine solubility of formaldehyde in absolute ethanol.

4 Conclusions

In this work, we prepared a tremella-like mesoporous CSH (AP-CSH) with a facile hydrothermal strategy. The structure and morphology of AP-CSH were characterized by XRD, FT-IR, SEM, elemental and nitrogen adsorption-desorption analyses. The results show that AP-CSH with multi-pleated surface structure has a high Ca/Si ratio (1.95), a large spe-
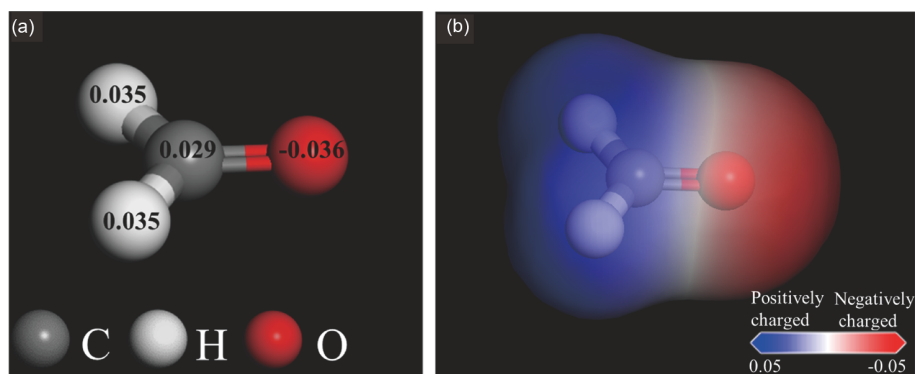
Figure 12   (Color online) Quantum chemical descriptors of formaldehyde. (a) Mulliken charge; (b) molecular electrostatic potential map.
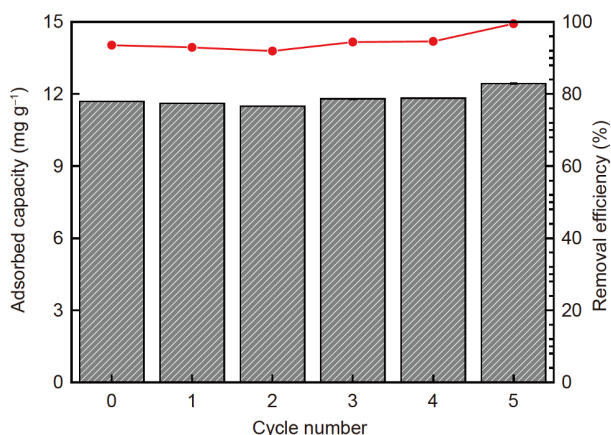

Figure 13   (Color online) Removal efficiency of AP-CSH and residual formaldehyde concentration during five adsorption-adsorption cycles (adsorption: m=0.4 g/50 mL; t=120 min and T=25°C. Desorption: eluent, absolute ethanol; v=5 mL, t=15 min and T=25°C).

cific surface area of 122.83 m^2 g^{-1}, and a pore size distribution range from 4 to 36 nm. With formaldehyde from aqueous solution as the target adsorbate, the adsorption capacity of AP-CSH was studied. The adsorption process was also investigated by adsorption kinetics and thermodynamics models. Results show that AP-CSH has excellent adsorption capacity, and can remove formaldehyde from water rapidly and effectively with the maximum removal efficiency of 98.94%. The adsorption process agrees well with the pseudo-second-order and Freundlich isotherm models. The experimental analyses and molecular dynamics simulation were conducted to investigate the adsorption mechanism. The appearance of new calcite phase and the changes of chemical shift from the analyses of XRD and XPS prove that the removal mechanism of formaldehyde by AP-CSH belongs to chemisorption. The first interaction peak at 2.83 Å in RDF curve of Si–O and the notably negative value of $E_{adsorption}$ (-98.24 kJ mol^{-1}) from molecular dynamics simulation indicate the formation of new bonding in the chemisorption process. Furthermore, AP-CSH maintains the extraordinary regeneration ability, which could recover the adsorption ac-

tivity only by simple immersion in absolute ethanol. After five regenerating cycles, the removal efficiency of formaldehyde remains about 99.50%. All the experimental results demonstrate that AP-CSH is an excellent adsorbent and has important application value in the adsorption field.

1   Gupta K, Khatri O P. Fast and efficient adsorptive removal of organic dyes and active pharmaceutical ingredient by microporous carbon: Effect of molecular size and charge. Chem Eng J, 2019, 378: 122218

2   Yitbarek M, Abdeta K, Beyene A, et al. Experimental evaluation of sorptive removal of fluoride from drinking water using natural and brewery waste diatomite. Process Saf Environ Protection, 2019, 128: 95–106

3   Keawkumay C, Rongchapo W, Sosa N, et al. Paraquat adsorption on NaY zeolite at various Si/Al ratios: A combined experimental and computational study. Mater Chem Phys, 2019, 238: 121824

4   Lin Z J, Zheng H Q, Zeng Y N, et al. Effective and selective adsorption of organoarsenic acids from water over a Zr-based metal-organic framework. Chem Eng J, 2019, 378: 122196

5   Maya F, Palomino Cabello C, Frizzarin R M, et al. Magnetic solid-phase extraction using metal-organic frameworks (MOFs) and their derived carbons. TrAC Trends Anal Chem, 2017, 90: 142–152

6   Niuniavaite D, Baltakys K, Dambrauskas T, et al. Cu^{2+}, Co^{2+} and Cr^{3+} adsorption by synthetic dibasic calcium silicate hydrates and their thermal stability in a 25–1000°C temperature range. J Therm Anal Calorim, 2019, 138: 2241–2249

7   Zhou Y, Hou D, Jiang J, et al. Experimental and molecular dynamics studies on the transport and adsorption of chloride ions in the nanopores of calcium silicate phase: The influence of calcium to silicate ratios. Microporous Mesoporous Mater, 2018, 255: 23–35

8   Uchima J S, Restrepo-Baena O J, Tobón J I. Mineralogical evolution of portland cement blended with metakaolin obtained in simultaneous calcination of kaolinitic clay and rice husk. Construct Build Mater, 2016, 118: 286–293

9   Guan W, Tian S. The internal recycle reactor enhances porous calcium silicate hydrates to recover phosphorus from aqueous solutions. J Chem, 2017, 2017: 2139594

10   Nielsen G D, Wolkoff P. Cancer effects of formaldehyde: A proposal for an indoor air guideline value. Arch Toxicol, 2010, 84: 423–446

11   Daoud Agha Dit Daoudy B, Al-Khayat M A, Karabet F, et al. A robust

static headic headspace GC-FID method to detect and quantify formaldehyde impurity in pharmaceutical excipients. J Anal Methods Chem, 2018, 2018: 4526396

12　Kaczala F, Marques M, Hogland W. Biotreatability of wastewater generated during machinery washing in a wood-based industry: COD, formaldehyde and nitrogen removal. Bioresour Tech, 2010, 101: 8975–8983

13　Naushad M, Ahamad T, Alothman Z A, et al. Synthesis, characterization and application of curcumin formaldehyde resin for the removal of Cd^{2+} from wastewater: Kinetics, isotherms and thermodynamic studies. J Indust Eng Chem, 2015, 29: 78–86

14　Nowshad F, Islam M N, Khan M S. Concentration and formation behavior of naturally occurring formaldehyde in foods. Agric Food Secur, 2018, 7: 17–25

15　Raskó J, Kecskés T, Kiss J. Adsorption and reaction of formaldehyde on TiO_2-supported Rh catalysts studied by FTIR and mass spectrometry. J Catal, 2004, 226: 183–191

16　Pásztory Z, Halász K, Börcsök Z. Formaldehyde adsorption-desorption of poplar bark. Bull Environ Contam Toxicol, 2019, 103: 745–749

17　Zvulunov Y, Ben-Barak-Zelas Z, Fishman A, et al. A self-regenerating clay-polymer-bacteria composite for formaldehyde removal from water. Chem Eng J, 2019, 374: 1275–1285

18　Downs R T, Hall-Wallace M. The *American Mineralogist* crystal structure database. Am Mineral, 2003, 88: 247–250

19　Guan W, Zhao X. Fluoride recovery using porous calcium silicate hydrates via spontaneous Ca^{2+} and OH^- release. Separation Purification Tech, 2016, 165: 71–77

20　Lü L N, Ping B, He Y J, et al. Effect of polymer on morphology and structure of calcium silicate hydrate prepared via precipitation method. J Wuhan Univ Technol-Mat Sci Edit, 2014, 29: 504–506

21　Liu R F, Li W B, Peng A Y. A facile preparation of TiO_2/ACF with C–Ti bond and abundant hydroxyls and its enhanced photocatalytic activity for formaldehyde removal. Appl Surf Sci, 2018, 427: 608–616

22　Li C X, Zhong H, Wang S, et al. Preparation of MnO_2 and calcium silicate hydrate from electrolytic manganese residue and evaluation of adsorption properties. J Cent South Univ, 2015, 22: 2493–2502

23　Si Q S, Zhu Q, Xing Z P. Simultaneous removal of nitrogen and phosphorus by magnesium-modified calcium silicate core-shell material in water. Ecotoxicol Environ Saf, 2018, 163: 656–664

24　Zhou Y, Hou D S, Jiang J Y, et al. Chloride ions transport and adsorption in the nano-pores of silicate calcium hydrate: Experimental and molecular dynamics studies. Construct Build Mater, 2016, 126: 991–1001

25　García Lodeiro I, Macphee D E, Palomo A, et al. Effect of alkalis on fresh C-S-H gels. FTIR analysis. Cement Concrete Res, 2009, 39: 147–153

26　Li X J, Wang Z M, Liang H J, et al. Chitosan modification persimmon tannin bioadsorbent for highly efficient removal of Pb(II) from aqueous environment: The adsorption equilibrium, kinetics and thermodynamics. Environ Tech, 2019, 40: 112–124

27　Liu S L, Li S, Niu H Y, et al. Facile synthesis of novel flowerlike magnetic mesoporous carbon for efficient chlorophenols removal. Microporous Mesoporous Mater, 2014, 200: 151–158

28　Rathore A S, Gupta G K, Kapur M, et al. Study on mass transfer characteristics for Cr (VI) removal by adsorption onto residual black toner ink. Environ Prog Sustain Energy, 2017, 36: 1022–1029

29　Chowdhury S, Mishra R, Saha P, et al. Adsorption thermodynamics, kinetics and isosteric heat of adsorption of malachite green onto chemically modified rice husk. Desalination, 2011, 265: 159–168

30　Zeng H H, Wang L, Zhang D, et al. Highly efficient and selective removal of mercury ions using hyperbranched polyethylenimine functionalized carboxymethyl chitosan composite adsorbent. Chem Eng J, 2019, 358: 253–263

31　Yang J B, Yu M Q, Qiu T. Adsorption thermodynamics and kinetics of Cr(VI) on KIP210 resin. J Industrial Eng Chem, 2014, 20: 480–486

32　Ozdes D, Gundogdu A, Kemer B, et al. Removal of Pb(II) ions from aqueous solution by a waste mud from copper mine industry: Equilibrium, kinetic and thermodynamic study. J Hazard Mater, 2009, 166: 1480–1487

33　Munagapati V S, Kim D S. Equilibrium isotherms, kinetics, and thermodynamics studies for congo red adsorption using calcium alginate beads impregnated with nano-goethite. Ecotoxicol Environ Saf, 2017, 141: 226–234

34　Braïda B Ã, Hiberty P C. Explicit solvation effects on the conventional resonance model for protonated imine, carbonyl, and thiocarbonyl compounds. Int J Quantum Chem, 2010, 110: 571–577

35　Igberase E, Osifo P, Ofomaja A. Adsorption of metal ions by microwave assisted grafting of cross-linked chitosan beads. Equilibrium, isotherm, thermodynamic and desorption studies. Appl Organometal Chem, 2018, 32: e4131

36　Kusrini E, Usman A, Sani F A, et al. Simultaneous adsorption of lanthanum and yttrium from aqueous solution by durian rind biosorbent. Environ Monit Assess, 2019, 191: 488

37　Huang X L, Huang Y, Pan Z, et al. Tailored high mesoporous activated carbons derived from Lotus seed shell using one-step $ZnCl_2$-activated method with its high Pb(II) capturing capacity. Environ Sci Pollut Res, 2019, 26: 26517–26528

38　Yan Z X, Xu Z H, Yu J G, et al. Effect of microstructure and surface hydroxyls on the catalytic activity of Au/AlOOH for formaldehyde removal at room temperature. J Colloid Interface Sci, 2017, 501: 164–174

39　Ježo L, Palou M, Kozánková J, et al. Determination of activation effect of $Ca(OH)_2$ upon the hydration of BFS and related heat by isothermal calorimeter. J Therm Anal Calorim, 2010, 101: 585–593

40　Bekçi Z, Seki Y, Kadir Yurdakoç M. A study of equilibrium and FTIR, SEM/EDS analysis of trimethoprim adsorption onto K10. J Mol Structure, 2007, 827: 67–74

41　Xu Y Q, Zhou G W, Wu C C, et al. Improving adsorption and activation of the lipase immobilized in amino-functionalized ordered mesoporous SBA-15. Solid State Sci, 2011, 13: 867–874

42　Xie Z, Cao S, Wang J, et al. Engineering of silicon-based ceramic fibers: Novel SiTaC(O) ceramic fibers prepared from polytantalosilane. Mater Sci Eng-A, 2010, 527: 7086–7091

43　Song X N, Meng T, Deng Y M, et al. The effects of the functional electrolyte additive on the cathode material $Na_{0.76}Ni_{0.3}Fe_{0.4}Mn_{0.3}O_2$ for sodium-ion batteries. Electrochim Acta, 2018, 281: 370–377

44　Zhang W, Du K Q, Yan C W, et al. Preparation and characterization of a novel Si-incorporated ceramic film on pure titanium by plasma electrolytic oxidation. Appl Surf Sci, 2008, 254: 5216–5223

45　Hu K, Zhuang J, Ding J, et al. Influence of biomacromolecule DNA corrosion inhibitor on carbon steel. Corrosion Sci, 2017, 125: 68–76

46　Jing Y, Wei L, Wang Y, et al. Molecular simulation of MCM-41: Structural properties and adsorption of CO_2, N_2 and flue gas. Chem Eng J, 2013, 220: 264–275

47　Xie S W, Liu Z, Han G C, et al. Molecular dynamics simulation of inhibition mechanism of 3,5-dibromo salicylaldehyde Schiff's base. Comput Theor Chem, 2015, 1063: 50–62

48　Fan B M, Ma Y C, Wang M M, et al. Revealing the assembly mechanism of an octadecylamine based supramolecular complex on mild steel in condensate water: Correlative experimental and theoretical studies. J Mol Liquids, 2019, 292: 111446

49　Esrafili M D, Dinparast L. The selective adsorption of formaldehyde and methanol over Al- or Si-decorated graphene oxide: A DFT study. J Mol Graphics Model, 2018, 80: 25–31

50　Alsbaiee A, Smith B J, Xiao L, et al. Rapid removal of organic micropollutants from water by a porous β-cyclodextrin polymer. Nature, 2016, 529: 190–194